Synergistic Metal-Support Interactions in Au/GaN Catalysts for Photoelectrochemical Nitrate Reduction to Ammonia

Wan Jae Dong,[1,2,‡] Jan Paul Menzel,[3,‡] Zhengwei Ye,[1] Zhuoran Long,[3] Ishtiaque Ahmed Navid,[1] Victor S. Batista,[3,*] and Zetian Mi[1,*]

[1] Department of Electrical Engineering and Computer Science, University of Michigan, 1301 Beal Avenue, Ann Arbor, Michigan 48109, USA

[2] Department of Integrative Energy Engineering, Graduate School of Energy and Environment (KU-KIST Green School), College of Engineering, Korea University, Seoul 02841, Republic of Korea.

[3] Department of Chemistry, Yale University, New Haven, Connecticut 06520-8107, USA

[‡]W. J. Dong and J. P. Menzel contributed equally to this work.

[*]E-mail: ztmi@umich.edu, victor.batista@yale.edu

METHODS

Preparation of GaN nanowires on n^+-p Si wafer

The n^+-p silicon junction was firstly fabricated through a standard thermal diffusion process using a (100) silicon wafer. Phosphorus dopant was deposited on the front side of the polished p-Si (100) wafer by spin-coating. It was then annealed at 950 ºC under nitrogen atmosphere for 4 h. Plasma-assisted molecular-beam epitaxy was used for growing n-type GaN NWs on silicon wafer under nitrogen-rich condition to promote the formation of an N-terminated surface to protect against photocorrosion and oxidation. The substrate temperature was 790 ºC and the growth duration was ~2 h. The forward plasma power was 350 W with Ga flux beam equivalent pressure (BEP) of 5×10^{-8} Torr.

Loading of Au NCs on GaN/Si

Au NCs were loaded on GaN/Si by a photodeposition method. GaN/Si wafer on a Teflon holder was put in the bottom of a reactor containing 66 mL of 20 vol% methanol aqueous solution. Then, 1, 10, and 100 µl of 0.4 M $HAuCl_4$ (Sigma-Aldrich) was added into the chamber to obtain Au1/GaN/Si, Au10/GaN/Si, and Au100/GaN/Si photoelectrodes, respectively. The reactor was covered by a quartz lid and evacuated for 5 min using a rotary pump. A 300 W Xe lamp (Cermax, PE300BUV) was adopted as a light source which irradiated the chamber for 30 min. Au ions were reduced and deposited onto GaN NWs during light illumination. After the photodeposition, the samples were rinsed with deionized water and dried by air blowing.

Characterization

The scanning electron microscopy (SEM) was performed using a field-emission scanning electron microscope (MIRA3 TESCAN) with 10 kV acceleration voltage and 15 mm working distance. The scanning-transmission electron microscopy (STEM) and energy dispersive X-ray spectroscopy (EDS) images were collected at 200 kV using JEOL 3100R05 Double Cs Corrected TEM/STEM with a 200 kV accelerating voltage which generated the high-resolution transmission electron microscopy (HRTEM) and high-angle annular dark field scanning transmission electron microscopy (HAADF-STEM) images. The X-ray photoelectron spectroscopy (XPS) was measured using a Kratos Axis Ultra XPS with a monochromatic Al Kα source. The X-ray diffraction (XRD) patterns were collected on a Rigaku X-ray diffractometer equipped with Cu Kα radiation. The *In-situ* infrared

spectroscopy of nitrate reduction was performed on an INVENIO-R Fourier transform infrared spectrometer (FT-IR) equipped with a mercury cadmium telluride (MCT) detector. The IR spectra were further converted to Kubelka-Munk unit using Omnic™ software.

Photoelectrochemical measurements

All photoelectrochemical measurements were conducted in an H-type cell separated by a Nafion membrane with a three-electrode system using a potentiostat. Ag/AgCl filled with 3 M KCl was used for the reference electrode and Pt wire was used for the counter electrode. Au/GaN/Si as well as other photoelectrodes were used as the working electrodes. The measured potentials ($V_{Ag/AgCl}$) (V) were converted to the reversible hydrogen electrode (V_{RHE}) (V) by using the Nernst function: $V_{RHE} = V_{Ag/AgCl} + 0.197 + 0.0591 \times pH$. The electrolytes were aqueous solutions of 0.1 M K_2SO_4 (Sigma-Aldrich) with different KNO_3 (Sigma-Aldrich) concentrations of 0, 0.02, 0.1, 0.5, and 1 M prepared by dissolving the solid salts in deionized water. pH values of electrolytes were measured using a pH meter (Mettler Toledo). The electrolyte volume in the two compartments of H-cell was 8 ml and was purged with Ar for 30 min before the measurement. The light source used for the illumination was LCS-100 (ORIEL) and the light intensity with AM 1.5G filter was calibrated by adjusting the distance from the sample to the light source. LSV curves were recorded at a rate of 10 mV/s. All measurements were conducted at ambient pressure and room temperature. After the reaction, the electrolyte was collected and NH_3, NO_2^-, and N_2H_4 products were analyzed by UV-Vis spectrophotometry. H_2 product was analyzed using gas chromatography (Shimadzu GC-8A) equipped with a thermal conductivity detector. 1 ml of gas product in the reaction chamber was injected into the gas chromatographs for analysis.

Determination of NH_3

The concentration of NH_3 product was spectrocolorimetrically determined by the indophenol blue method. A certain amount of electrolyte was taken out from the cathodic compartment and diluted. Subsequently, 1 ml of a 1 M NaOH (Sigma-Aldrich) solution containing 5 wt% salicylic acid (Sigma-Aldrich) and 5 wt% sodium citrate (Sigma-Aldrich) was added to the 1 ml of diluted electrolyte, followed by the addition of 0.5 ml of 0.05M NaClO (Sigma-Aldrich) and 0.1 ml of 1 wt% $C_5FeN_6Na_2O$ (Sigma-Aldrich) solution. The solution was stored more than 2 h in dark before the UV-vis measurement (Varian 50-Bio). The concentration of NH_3 was determined by absorbance at a wavelength of 655 nm. For the

calibration, NH_4Cl (Sigma-Aldrich) standard solutions with known concentration was used.

Determination of NO_2^-

0.2 g of N-(1-naphthyl) ethylenediamine dihydrochloride (Sigma-Aldrich), 4 g of p-aminobenzenesulfonamide (Sigma-Aldrich), and 10 ml of phosphoric acid (Sigma-Aldrich) were added into 50 ml of deionized water as the color reagent. Then 2.5 ml of the diluted electrolyte were mixed with 0.05 ml of color reagent. The absorbance at a wavelength of 540 nm was collected by UV-vis spectrometer to determinte the concentration of NO_2^-. For the calibration, KNO_2 (Sigma-Aldrich) standard solutions with known concentration was used.

Determination of N_2H_4

1.5 g of $C_9H_{11}NO$ (Sigma-Aldrich) and 7.5 ml of HCl (Sigma-Aldrich) were added into 75 ml of ethanol (Sigma-Aldrich) as the color agent. Then 1 ml of the electrolyte was mixed with 1 mL of color reagent. The absorbance at a wavelength of 455 nm was collected by UV-vis spectrometer to determinte the concentration of N_2H_4. For the calibration, hydrazine hydrate (Sigma-Aldrich) standard solutions with known concentration was used.

Calculation of faradaic efficiency and production rate

The faradaic efficiency (FE) of NO_3^- reduction reaction was calculated as follows:

$$FE_{NH3} = \frac{8 \times F \times C_{NH3} \times V}{17 \times Q}$$

$$FE_{NO2-} = \frac{2 \times F \times C_{NO2-} \times V}{46 \times Q}$$

$$FE_{N2H4} = \frac{14 \times F \times C_{N2H4} \times V}{32 \times Q}$$

The produdction rate of each product of NH_3, NO_2^-, and N_2H_4 was calculated using the following equation:

$$Y_{NH3} = \frac{C_{NH3} \times V}{17 \times t \times A}$$

$$Y_{NO2-} = \frac{C_{NO2-} \times V}{46 \times t \times A}$$

$$Y_{N2H4} = \frac{C_{N2H4} \times V}{32 \times t \times A}$$

Where F is the Faraday constant (96,485 C/mol), V is the volume of the cathoid electrolyte (8 ml), Q is the total charge flowed, t is the reaction time, and A is the geometric surface area

of photoelectrodes. C_{NH3}, C_{NO2-}, and C_{N2H4} are the measured NH_3, NO_2^-, and N_2H_4 concentrations, respectively.

Computational Details

DFT based meahcnistic studies were performed using the VASP.5 program,[1] using the PBE functional [2] with D3 dispersion corrections including BJ damping.[3] The core electrons were described using Projected-augmented Wave potentials (PAW).[4] Using the optimized gold bulk geometry, the Au(211) surface was constructed including four layers of 3x3 Au atoms, with the lowest two layers frozen in bulk geometry while allowing the upper two layers adapt to the new surface environment. A 3x3x1 Monkhorst-Pack[5] type grid was used, with a cut-off energy of 450 eV. Geometries were converged until the forces were below 0.2 eV/Å with an energy convergence criterion of 10^{-6} eV. The optimization resulted in a surface structure with lattice vectors of a=7.103 Å, b=8.699 Å. In c, the box was extended to 40.00 Å to include a large vaccuum layer and prevent self interaction. The resulting simulation box is shown in Figure S20. All visualizations were done using the VESTA visualization program.[6] Frequency calculations were performed after optimization of the intermediates to determine free energy corrections, using the harmonic approximation. The vaspkit1.3[7] post-processing package was used with settings of 298 K and 1 atm pressure. Solvent corrections were added by performing a geometry optimization in implicit water, using the VASPSol[8] extension and a dielectric constant of 80. Free energies were calculated assuming the computational hydrogen electrode, equating the free energy of an electron and proton to equal to the free energy of half a hydrogen molecule. The free energies for Nitrate reduction on GaN were taken from reference.[9]

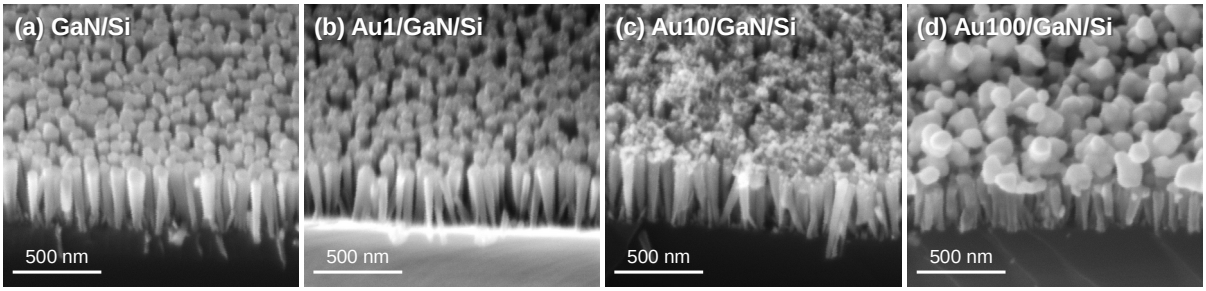

Figure S1. Tilted-view SEM images of (a) GaN/Si, (b) Au1/GaN/Si, (c) Au10/GaN/Si, and (d) Au100/GaN/Si. Au NCs were coated on the upper region of GaN NWs and their size increased with increasing the amount of 0.4 M $HAuCl_4$ precursor solution used for photodeposition process.

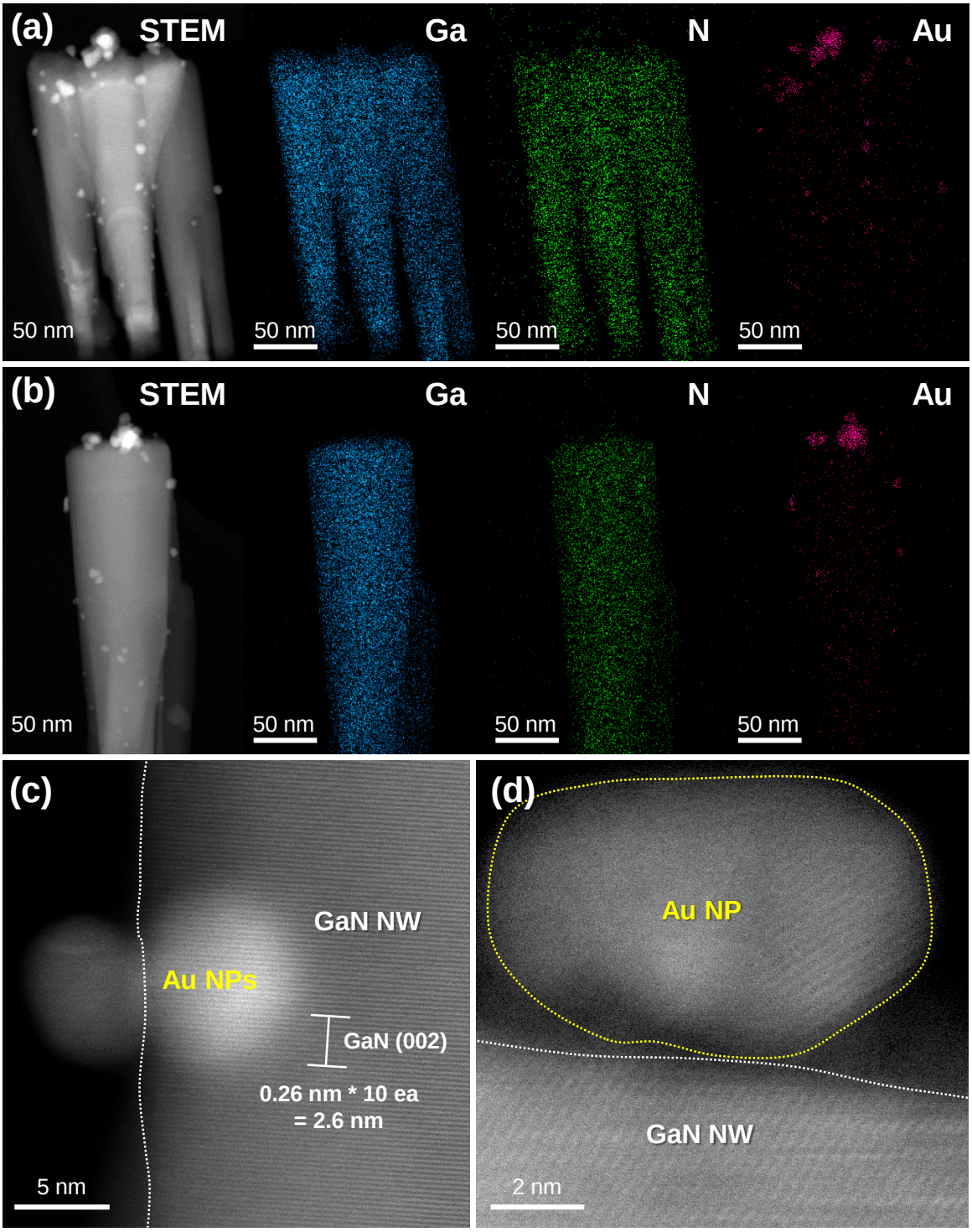

Figure S2. (a,b) STEM image and EDS elemental maps of Au10/GaN/Si. (c,d) High-resolution TEM images of Au NC/GaN NW interface. GaN NW was single crystal with growth direction of [002].

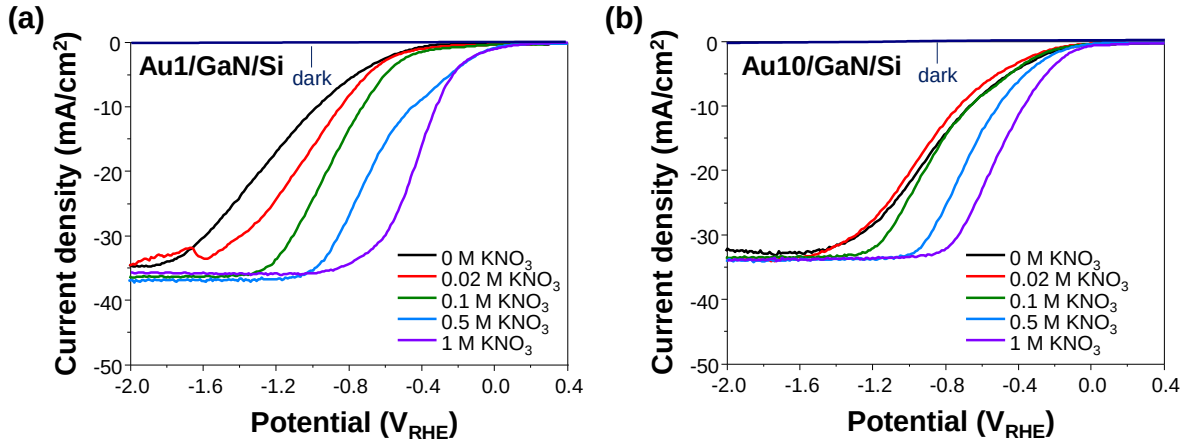

Figure S3. LSV curves of (a) Au1/GaN/Si and (b) Au10/GaN/Si in 0.1 M K_2SO_4 with KNO_3 concentrations of 0, 0.02, 0.1, 0.5, and 1 M. The measurement was conducted under AM 1.5G 1-sun light illumination. Under dark conditions, the photoelectrodes were tested in 0.1 M K_2SO_4 electrolyte.

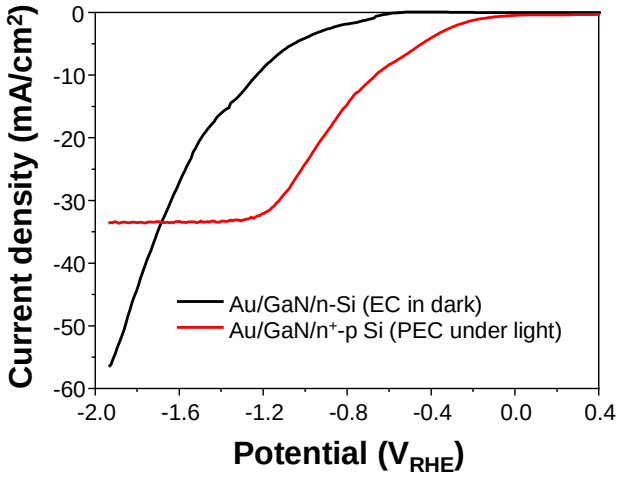

Figure S4. LSV curves of electrochemical reaction using Au10/GaN/n-Si in dark and photoelectrochemical reaction using Au10/GaN/n^+-p Si under illuminated condition, measured in 0.1 M K_2SO_4 with 0.1 M KNO_3 electrolyte.

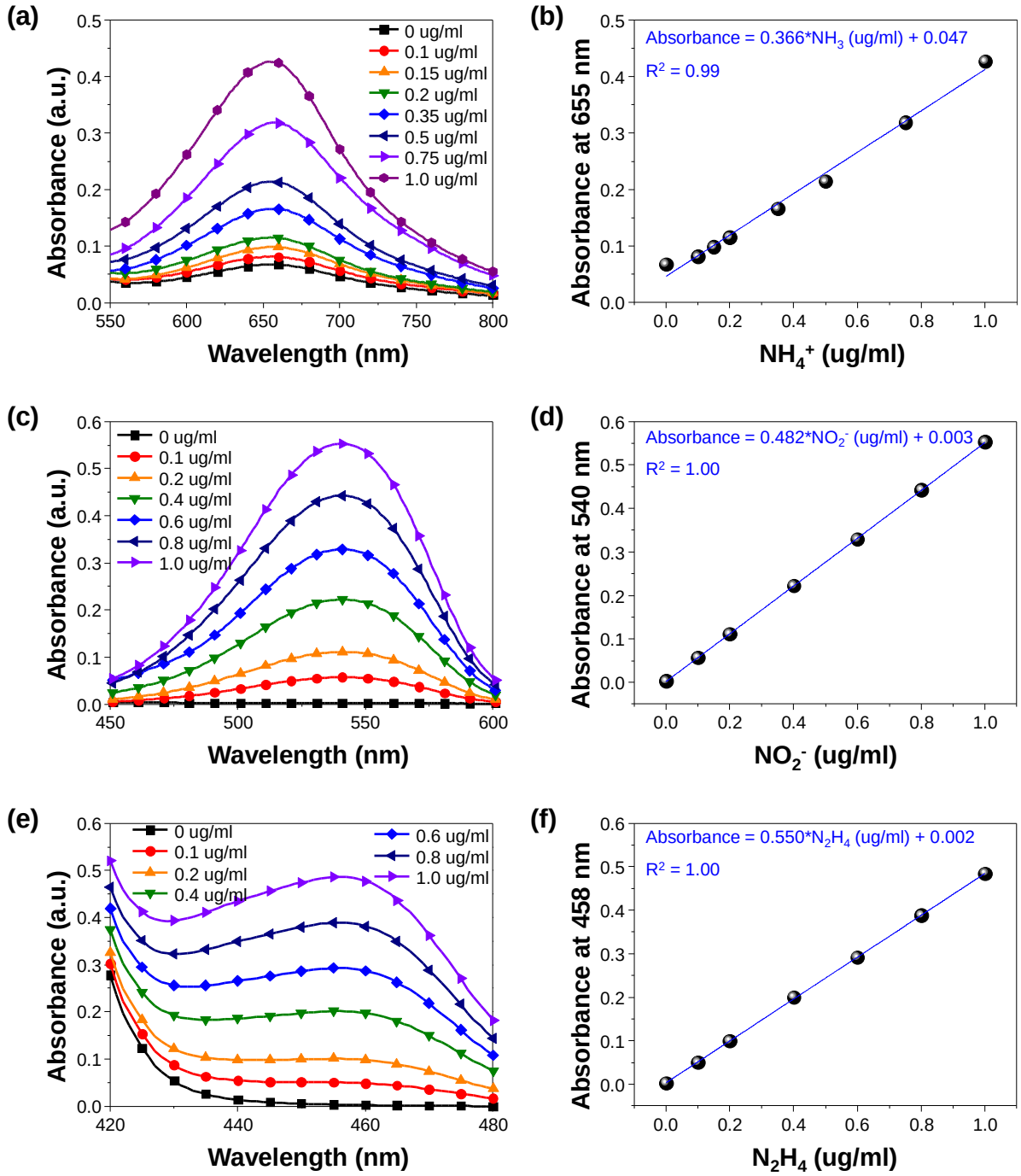

Figure S5. (a) UV-vis spectra of indophenol assays with NH_4^+ ions and (b) calibration curve of NH_4^+. (c) UV-vis spectra and (d) calibration curve of NO_2^-. (e) UV-vis spectra and (f) calibration curve of N_2H_4.

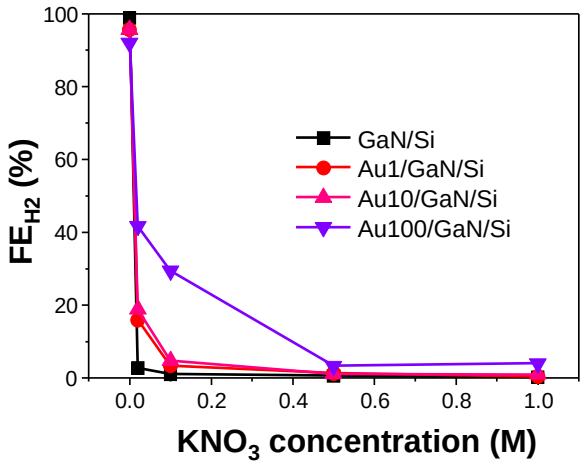

Figure S6. Faradaic efficiency of H_2 for GaN/Si, Au1/GaN/Si, Au10/GaN/Si, and Au100/GaN/Si measured in 0.1 M K_2SO_4 with different KNO_3 concentration at -0.4 V_{RHE}.

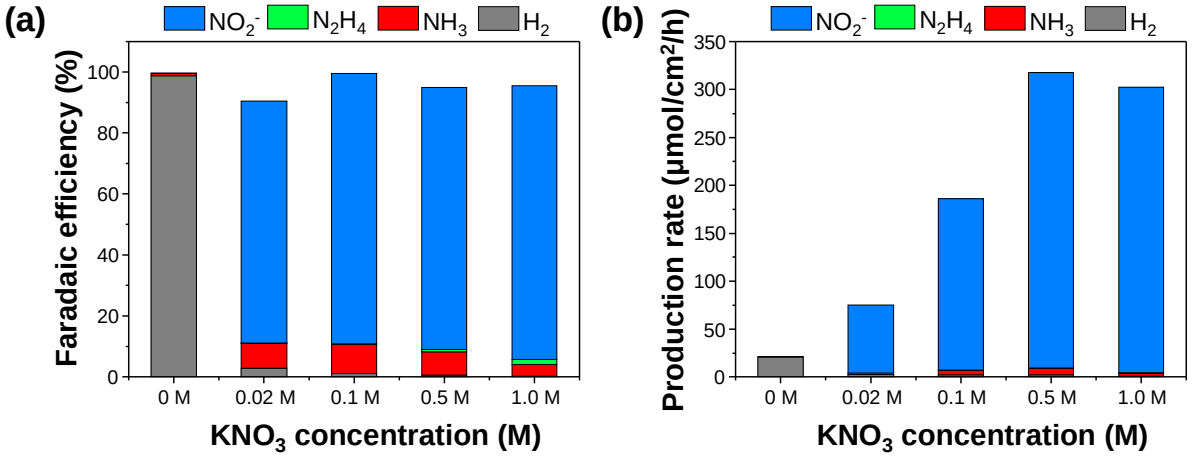

Figure S7. (a) Faradaic efficiency and (b) production rate of H_2, NH_3, NO_2^-, and N_2H_4 on GaN/Si in 0.1 M K_2SO_4 with KNO_3 concentrations of 0, 0.02, 0.1, 0.5, and 1 M at -0.4 V_{RHE}.

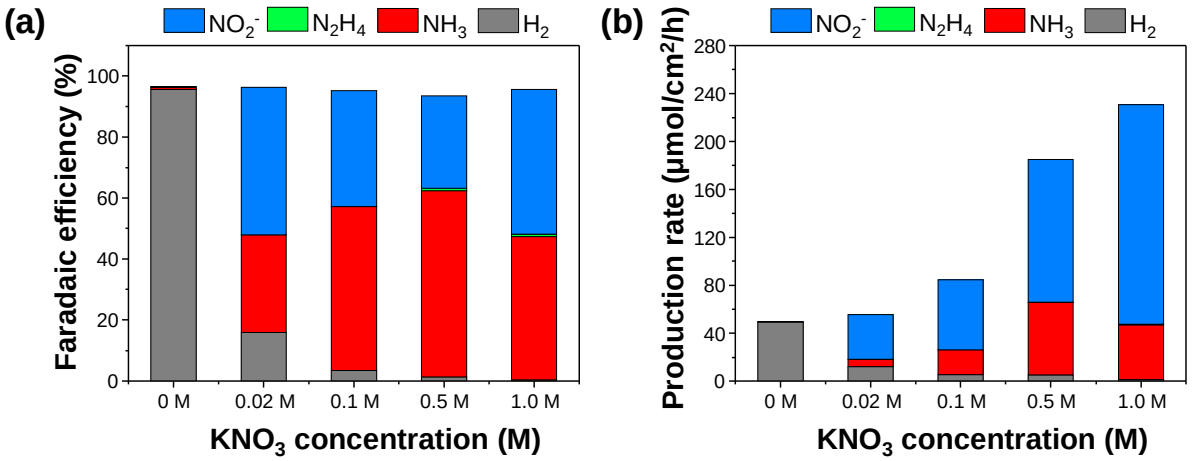

Figure S8. (a) Faradaic efficiency and (b) production rate of H_2, NH_3, NO_2^-, and N_2H_4 on Au1/GaN/Si in 0.1 M K_2SO_4 with KNO_3 concentrations of 0, 0.02, 0.1, 0.5, and 1 M at -0.4 V_{RHE}.

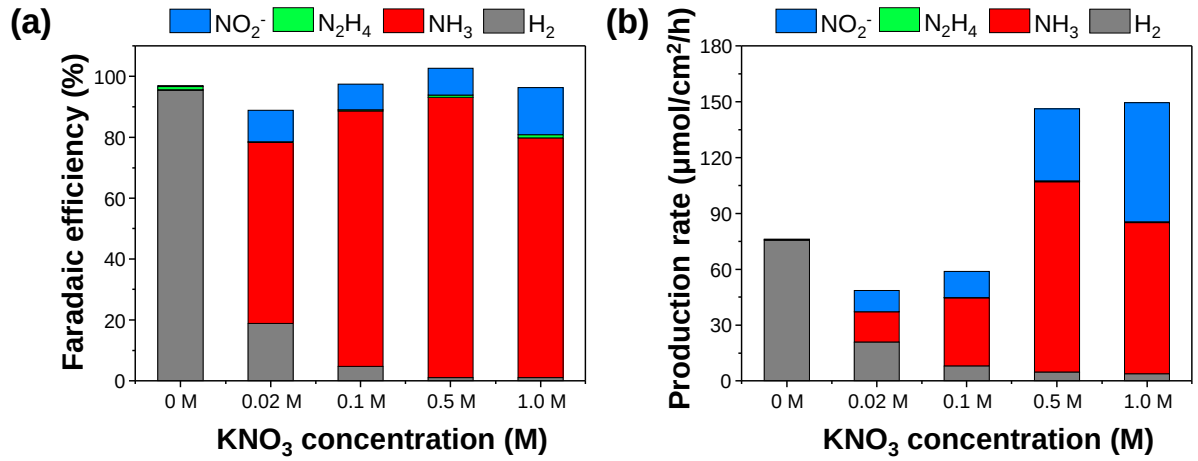

Figure S9. (a) Faradaic efficiency and (b) production rate of H_2, NH_3, NO_2^-, and N_2H_4 on Au10/GaN/Si in 0.1 M K_2SO_4 with KNO_3 concentrations of 0, 0.02, 0.1, 0.5, and 1 M at -0.4 V_{RHE}.

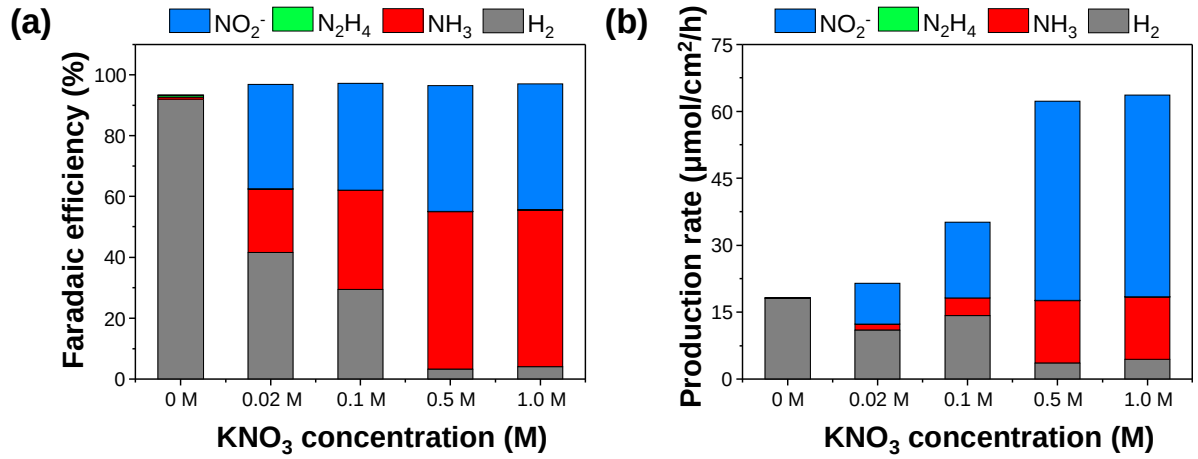

Figure S10. (a) Faradaic efficiency and (b) production rate of H_2, NH_3, NO_2^-, and N_2H_4 on Au100/GaN/Si in 0.1 M K_2SO_4 with KNO_3 concentrations of 0, 0.02, 0.1, 0.5, and 1 M at -0.4 V_{RHE}.

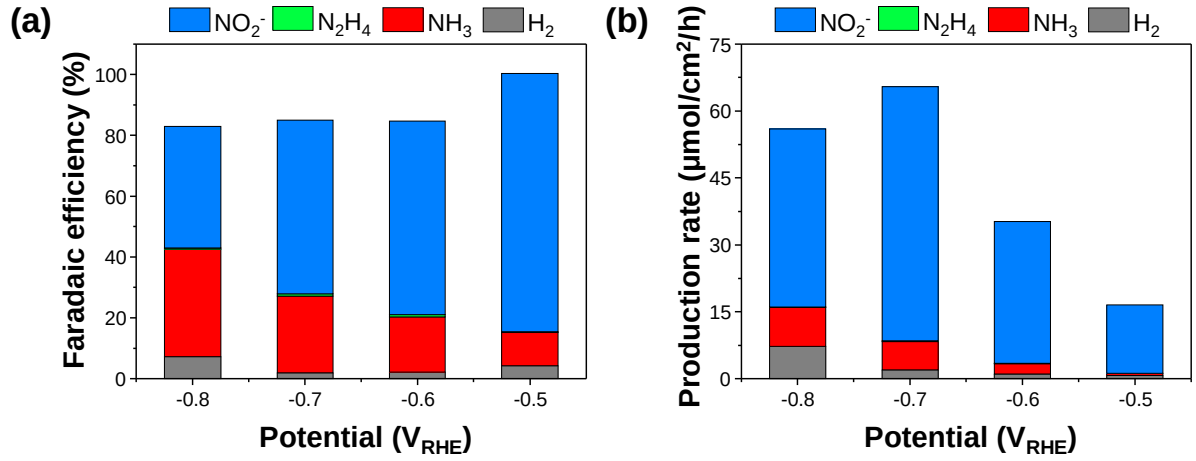

Figure S11. Potential-dependent (a) Faradaic efficiency and (b) production rate of H_2, NH_3, NO_2^-, and N_2H_4 on Si in 0.1 M K_2SO_4 with 0.5 M KNO_3 concentration. Cathodic potentials were varied from -0.5 to -0.8 V_{RHE}.

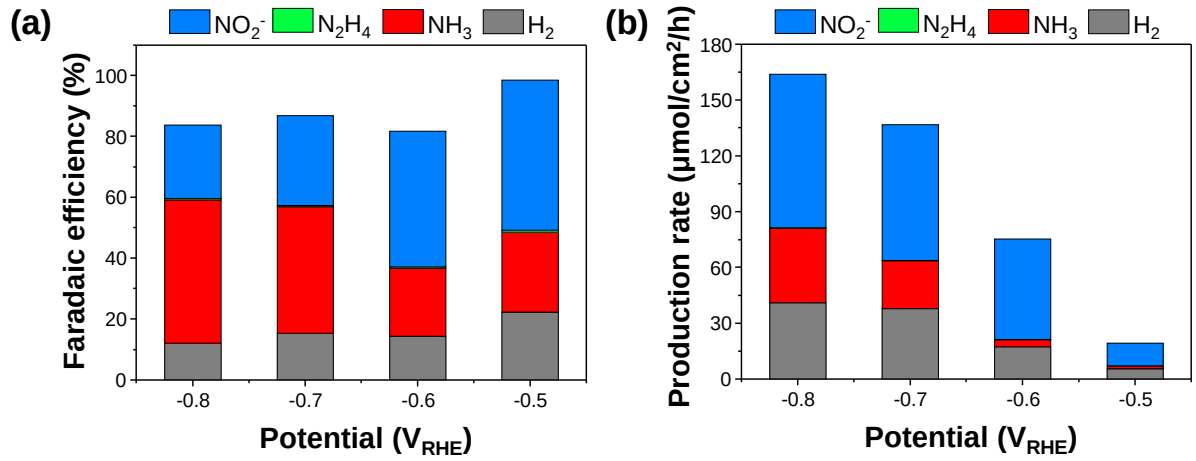

Figure S12. Potential-dependent (a) Faradaic efficiency and (b) production rate of H_2, NH_3, NO_2^-, and N_2H_4 on Au10/Si in 0.1 M K_2SO_4 with 0.5 M KNO_3 concentration. Cathodic potentials were varied from -0.5 to -0.8 V_{RHE}.

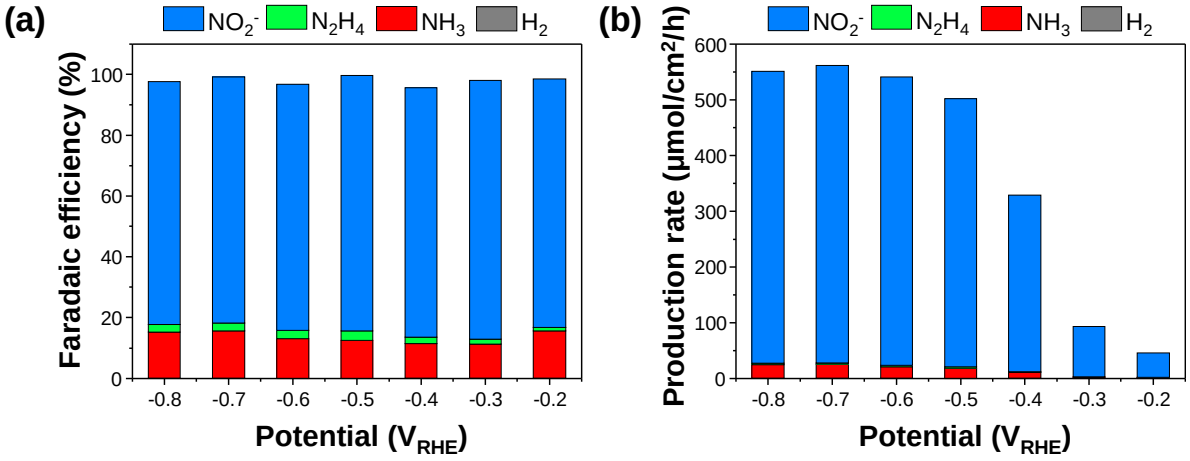

Figure S13. Potential-dependent (a) Faradaic efficiency and (b) production rate of H_2, NH_3, NO_2^-, and N_2H_4 on GaN/Si in 0.1 M K_2SO_4 with 0.5 M KNO_3 concentration. Cathodic potentials were varied from -0.2 to -0.8 V_{RHE}.

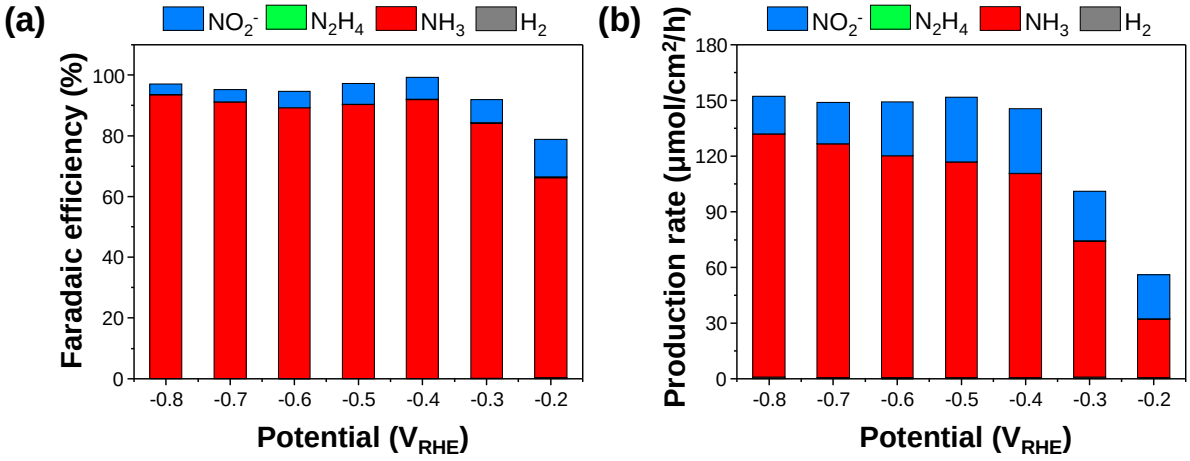

Figure S14. Potential-dependent (a) Faradaic efficiency and (b) production rate of H_2, NH_3, NO_2^-, and N_2H_4 on Au10/GaN/Si in 0.1 M K_2SO_4 with 0.5 M KNO_3 concentration. Cathodic potentials were varied from -0.2 to -0.8 V_{RHE}.

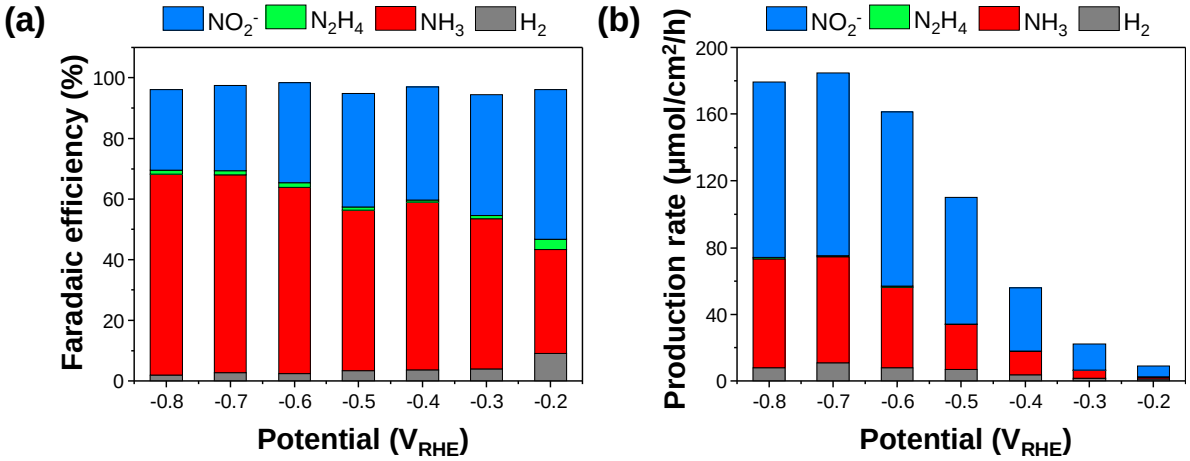

Figure S15. Potential-dependent (a) Faradaic efficiency and (b) production rate of H_2, NH_3, NO_2^-, and N_2H_4 on Au100/GaN/Si in 0.1 M K_2SO_4 with 0.5 M KNO_3 concentration. Cathodic potentials were varied from -0.2 to -0.8 V_{RHE}.

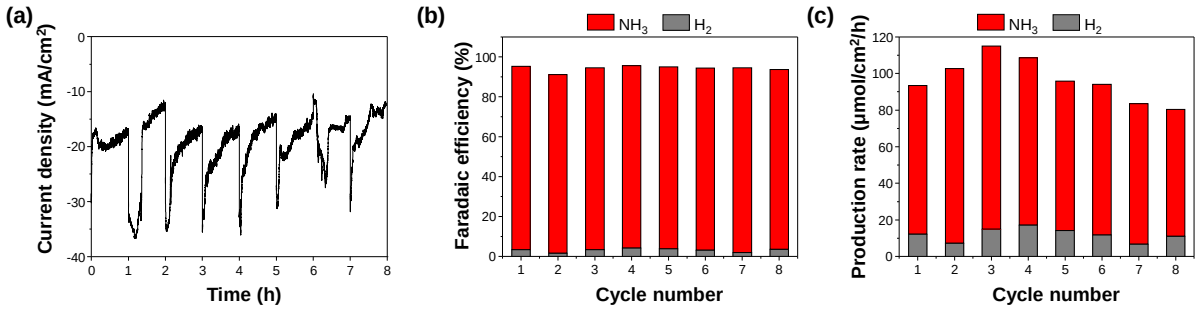

Figure S16. Stability test of Au10/GaN/Si in 0.1 M K_2SO_4 with 0.5 M KNO_3 at -0.4 V_{RHE}. (a) Chronoamperometric curve, (b) faradaic efficiency, and (c) production rate of H_2 and NH_3. Each cycle was performed for 1 h with repeated replacement of fresh electrolyte after each cycle.

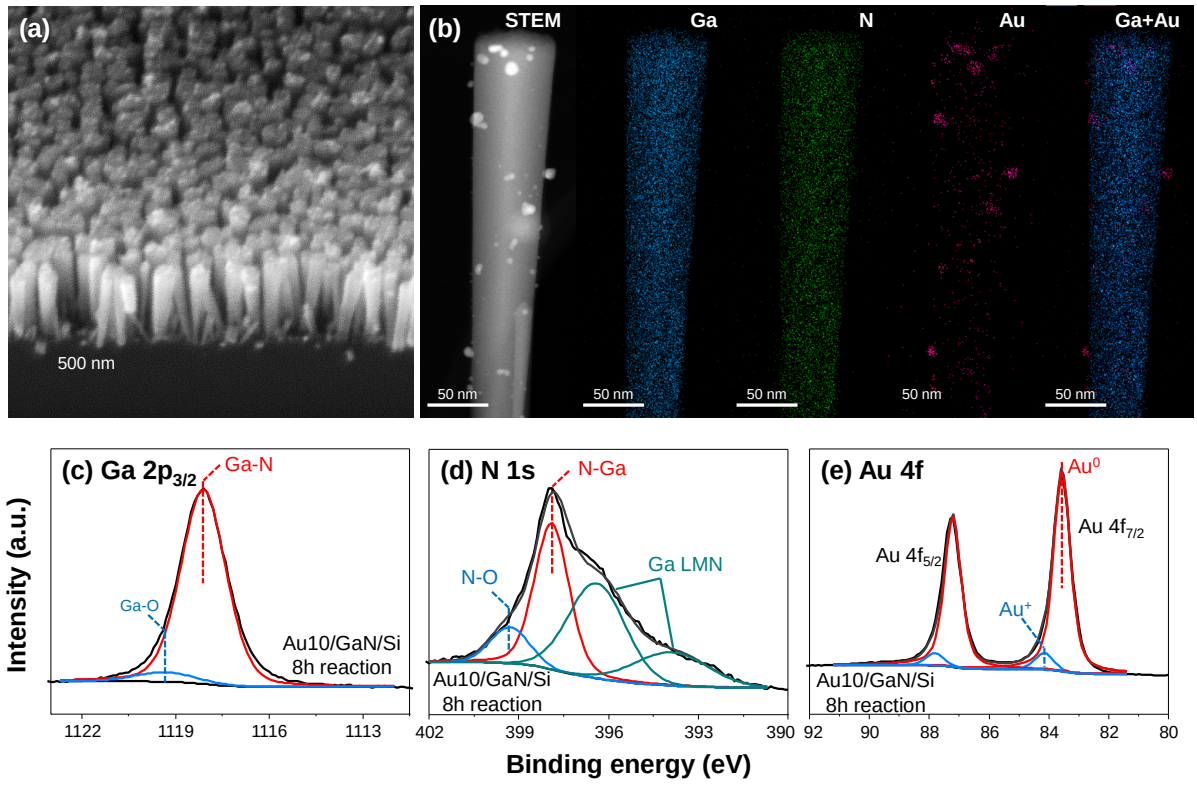

Figure S17. Material characterization of Au10/GaN/Si after 8 h reaction at -0.4 V_{RHE}. (a) Tilt-view SEM image and (b) STEM image and STEM-EDS elemental maps of Au10/GaN/Si. XPS spectra of (c) Ga $2p_{2/3}$, (d) N 1s, (e) Au 4f. Calculated Au/Ga+N atomic ratio was 0.47.

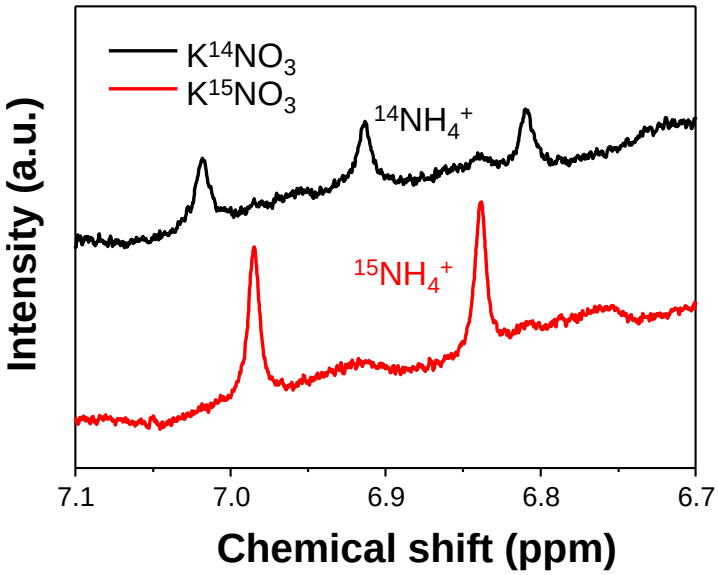

Figure S18. ^{1}H NMR spectra of the electrolytes after NO_3^- reduction reaction using $K^{14}NO_3$ and $K^{15}NO_3$ as the nitrogen source. Au10/GaN/Si was used in 0.1 M K_2SO_4 with 0.5 M KNO_3 at -0.4 V_{RHE}. Typical triple and double peaks of NH_4^+ were observed with reactants of $^{14}NO_3^-$ and $^{15}NO_3^-$, respectively.

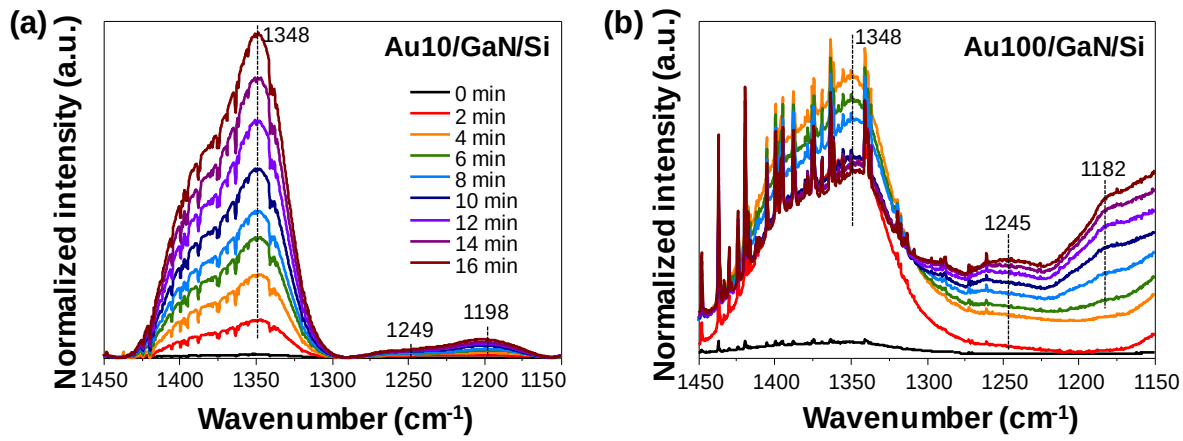

Figure S19. (a) *In-situ* IR spectra of NO_3^- reduction on (a) Au10/GaN/Si and (b) Au100/GaN/Si in 0.1 M K_2SO_4 with 0.5 M KNO_3 at -0.6 V_{RHE}.

To investigate the origin of NO_3^-RR activity on Au/GaN/Si, *in-situ* infrared (IR) measurements were performed in 0.1 M K_2SO_4 with 0.5 M KNO_3 at -0.6 V_{RHE} by identifying intermediates and products desorbed from the surface. During NO_3^-RR on Au10/GaN/Si, a peak at 1348 cm^{-1} increased, indicating the consumption of NO_3^- in the electrolyte (Figure S19a).[10] Additionally, weak bands at 1249 and 1198 cm^{-1} confirmed the production of small amounts of NO_2^- and NH_2, respectively.[11] In contrast, higher loading of Au NCs (Au100/GaN/Si) showed relatively weaker IR peak intensities, reflecting lower NO_3^-RR activity (Figure S19b). Interestingly, the bands for NO_2^- (1245 cm^{-1}) and NH_2 (1182 cm^{-1}) were more intense relative to the NO_3^- consumption peak (1348 cm^{-1}), suggesting that a significant portion of intermediates desorbed before NH_3 production.

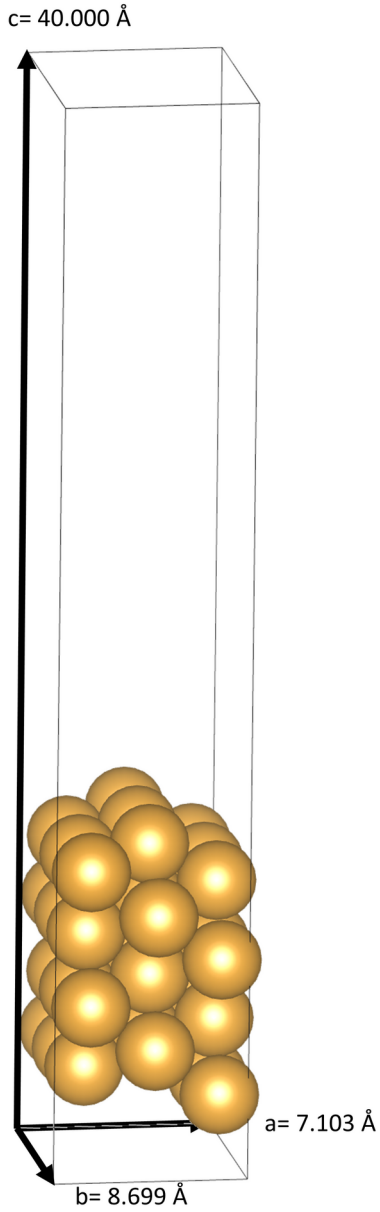

Figure S20. Simulation box of the Au (211) surface.

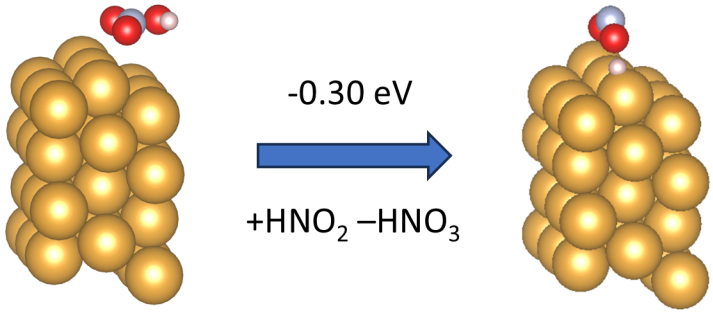

Figure S21. Chemisorption of HNO_3 vs HNO_2 on the step of the Au (211) surface.

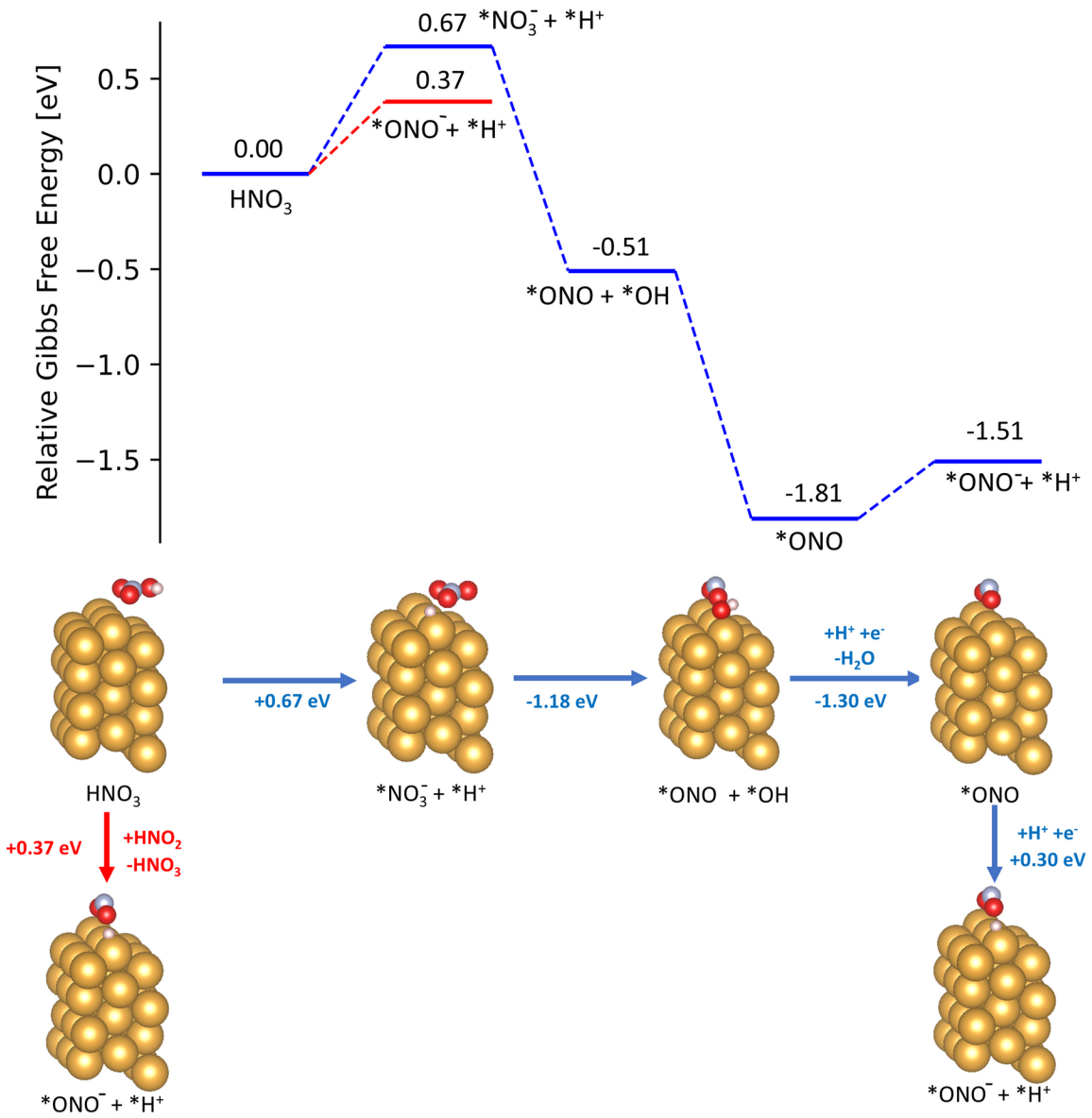

Figure S22. NO_3^- reduction on Au (211). In red, competing expulsion by NO_2^- is shown. Below, the DFT optimized structures are given.

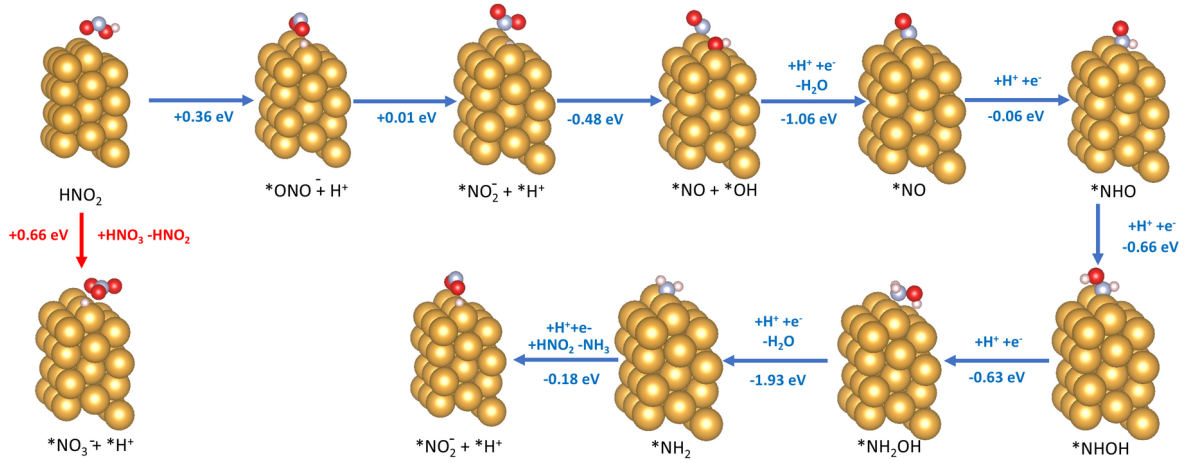

Figure S23. DFT optimized structures for NO_2^- reduction on Au (211). In red, the competing expulsion by NO_3^- is shown, which would lead to incomplete reduction remaining at NO_2^-.

Table S1. Performance and reaction condition comparison of electrochemical (EC) and photoelectrochemical (PEC) NO_3^- reduction from recent literature.

EC/ PEC	Cathode	Electrolyte	Potential	FE_{NH3}	Y_{NH3}	Ref.
EC	Cu-PTCDA	0.1 M PBS with 500 ppm $NaNO_3$	-0.4 V_{RHE}	85.9%	25.6 $\mu mol/cm^2/h$	S[12]
EC	CuNi alloy	0.1 M KOH with 0.1 M KNO_3	-0.15 V_{RHE}	99%	J_{NH3} = -90 mA/cm^2	S[13]
EC	Strained Ru nanocluster	1 M KOH with 1 M KNO_3	-0.2 V_{RHE}	~100%	1.17 $mmol/cm^2/h$	S[14]
EC	Cu/Cu_2O nanowire	0.5 M Na_2SO_4 with 200 ppm of $NaNO_3$	-0.85 V_{RHE}	95.8%	244.9 $\mu mol/cm^2/h$	S[15]
EC	Fe SAC	0.1 M K_2SO_4 with 0.5 KNO_3	-0.66 V_{RHE}	~75%	~121 $\mu mol/cm^2/h$	S[16]
EC	Fe-MoS_2	0.1 M $NaSO_4$ and 0.1 M NaOH with 0.1 $NaNO_3$	-0.48 V_{RHE}	98%	J_{NH3} = -8.4 mA/cm^2	S[17]
EC	Fe-PPy SACs	0.1 M KOH with 0.1 M KNO_3	-0.7 V_{RHE}	~100%	2.75 $mg_{NH3}/cm^2/h$	S[18]
EC	Oxide-derived Co	1 M KOH with 1 M KNO_3	-0.8 V_{RHE}	92.37%	J_{NH3} = -565.26 mA/cm^2	S[19]
EC	CuCoSP	0.1 M KOH with 0.1 M KNO_3	-0.175 V_{RHE}	93.3%	1.17 $mmol/cm^2/h$	S[20]
EC	Rh@Cu nanowire	0.1 M Na_2SO_4 with 0.1 M KNO_3	-0.2 V_{RHE}	93%	J_{NH3} = -162 mA/cm^2	S[11]
EC	Bi-Cl_{red}	1 M KOH with 0.5 M KNO_3	-0.5 V_{RHE}	90.6%	~11 $g_{NH3}/h/g_{cat}$	S[21]
EC	RhCu nanocube	0.01 M HClO4 with 0.05 M KNO_3	0.05 V_{RHE}	93.7%	2.4 $g_{NH3}/h/g_{cat}$	S[22]
EC	CoP nanosheet	1 M NaOH with 1 M $NaNO_3$	-0.3 V_{RHE}	~100%	956 $\mu mol/cm^2/h$	S[23]
EC	Pd-NDs/Zr-MOF	0.1 M Na_2SO_4 with 500 ppm $NaNO_3$	-1.3 V_{RHE}	58.1%	287.31 $mmol/h/g_{cat}$	S[24]
EC	$NiCo_2O_4$ nanowire	0.1 M NaOH with 0.1 M $NaNO_3$	-0.6 V_{RHE}	99%	973.2 $\mu mol/cm^2/h$	S[25]
PEC	O-SiNW/Au	0.5 M K_2SO_4 with 10 mM KNO_3	0.2 V_{RHE}	95.6%	0.26 $\mu mol/cm^2/h$	S[26]
PEC	Au/GaN/Si	0.1 M K_2SO_4 with 0.5 KNO_3	-0.4 V_{RHE}	91.8%	110 $\mu mol/cm^2/h$	This work

Table S2. Energies in implicit solvent, free energy corrections and Free energies of the reactants and products. Note that H_2 is calculated in vacuum.

Intermediate	Electronic energy [eV]	Free energy correction term [eV]	Gibbs free energy [eV]
HNO_3	-28.998	-0.010	-29.007
HNO_2	-23.098	-0.125	-23.222
H_2	-6.769	-0.023	-6.792
NH_3	-19.742	+0.422	-19.319
H_2O	-14.544	+0.087	-14.457

Table S3. Energies in implicit solvent, free energy corrections and Free energies of the adsorbed intermediates on Au (211).

Intermediate	Electronic energy [eV]	Free energy correction term [eV]	Gibbs free energy [eV]
Au(211)	-127.124	+0.000	-127.124
HNO_3 (physisorbed)	-156.479	+0.509	-155.970
HNO_2 (physisorbed)	-150.515	+0.338	-150.177
$*NO_3^- *H^+$	-155.680	+0.376	-155.304
*ONO *OH	-156.880	+0.402	-156.478
*ONO	-146.849	+0.130	-146.719
$*ONO^- H^+$	-150.083	+0.266	-149.816
$*NO_2^- H^+$	-150.107	+0.301	-149.806
*NO *OH	-150.657	+0.364	-150.293
*NO	-140.375	+0.081	-140.294
*NHO	-144.122	+0.367	-143.754
*NOH	-143.613	+0.366	-143.247
*NHOH	-148.530	+0.723	-147.807
$*NH_2O$	-148.093	+0.711	-147.382
$*NH_2OH$	-152.816	+0.984	-151.832
*NH	-138.053	+0.316	-137.736
$*NH_2$	-143.371	+0.671	-142.699

References

[1] a) G. Kresse, J. Hafner, *Physical Review B* **1993**, *47*, 558; b) G. Kresse, J. Furthmüller, *Physical Review B* **1996**, *54*, 11169; c) G. Kresse, J. Furthmüller, *Computational Materials Science* **1996**, *6*, 15-50.

[2] J. P. Perdew, K. Burke, M. Ernzerhof, *Physical Review Letters* **1996**, *77*, 3865.

[3] a)S. Grimme, J. Antony, S. Ehrlich, H. Krieg, *The Journal of Chemical Physics* **2010**, *132*; b) S. Grimme, S. Ehrlich, L. Goerigk, *Journal of Computational Chemistry* **2011**, *32*, 1456-1465.

[4] a) G. Kresse, J. Hafner, *Journal of Physics: Condensed Matter* **1994**, *6*, 8245; b) G. Kresse, D. Joubert, *Physical Review B* **1999**, *59*, 1758.

[5] H. J. Monkhorst, J. D. Pack, *Physical Review B* **1976**, *13*, 5188.

[6] K. Momma, F. Izumi, *Journal of Applied Crystallography* **2011**, *44*, 1272-1276.

[7] V. Wang, N. Xu, J.-C. Liu, G. Tang, W.-T. Geng, *Computer Physics Communications* **2021**, *267*, 108033.

[8] K. Mathew, R. Sundararaman, K. Letchworth-Weaver, T. Arias, R. G. Hennig, *The Journal of Chemical Physics* **2014**, *140*.

[9] W. J. Dong, J. P. Menzel, Z. Ye, I. A. Navid, P. Zhou, K. R. Yang, V. S. Batista, Z. Mi, *ACS Catalysis* **2024**, *14*, 2588-2596.

[10] E. Pérez-Gallent, M. C. Figueiredo, I. Katsounaros, M. T. Koper, *Electrochim. Acta* **2017**, *227*, 77-84.

[11] H. Liu, X. Lang, C. Zhu, J. Timoshenko, M. Rüscher, L. Bai, N. Guijarro, H. Yin, Y. Peng, J. Li, *Angew. Chem. Int. Ed.*, **2022,** *61*, e202202556.

[12] G.-F. Chen, Y. Yuan, H. Jiang, S.-Y. Ren, L.-X. Ding, L. Ma, T. Wu, J. Lu, H. Wang, *Nat. Energy* **2020**, *5*, 605-613.

[13] Y. Wang, A. Xu, Z. Wang, L. Huang, J. Li, F. Li, J. Wicks, M. Luo, D.-H. Nam, C.-S. Tan, *J. Am. Chem. Soc.* **2020**, *142*, 5702-5708.

[14] J. Li, G. Zhan, J. Yang, F. Quan, C. Mao, Y. Liu, B. Wang, F. Lei, L. Li, A. W. Chan, *J. Am. Chem. Soc.* **2020**, *142*, 7036-7046.

[15] Y. Wang, W. Zhou, R. Jia, Y. Yu, B. Zhang, *Angew. Chem. Int. Ed.* **2020**, *59*, 5350-5354.

[16] Z.-Y. Wu, M. Karamad, X. Yong, Q. Huang, D. A. Cullen, P. Zhu, C. Xia, Q. Xiao, M. Shakouri, F.-Y. Chen, *Nat. Commun.* **2021**, *12*, 1-10.

[17] J. Li, Y. Zhang, C. Liu, L. Zheng, E. Petit, K. Qi, Y. Zhang, H. Wu, W. Wang, A.

Tiberj, *Adv. Funct. Mater.* **2022**, *32*, 2108316.

[18] P. Li, Z. Jin, Z. Fang, G. Yu, *Energy Environ. Sci.* **2021**, *14*, 3522-3531.

[19] N. C. Kani, J. A. Gauthier, A. Prajapati, J. Edgington, I. Bordawekar, W. Shields, M. Shields, L. C. Seitz, A. R. Singh, M. R. Singh, *Energy Environ. Sci.* **2021**, *14*, 6349-6359.

[20] W. He, J. Zhang, S. Dieckhöfer, S. Varhade, A. C. Brix, A. Lielpetere, S. Seisel, J. R. Junqueira, W. Schuhmann, *Nat. Commun.* **2022**, *13*, 1-13.

[21] N. Zhang, J. Shang, X. Deng, L. Cai, R. Long, Y. Xiong, Y. Chai, *ACS Nano* **2022**, *16*, 4795-4804.

[22] Z. X. Ge, T. J. Wang, Y. Ding, S. B. Yin, F. M. Li, P. Chen, Y. Chen, *Adv. Energy Mater.* **2022**, 2103916.

[23] S. Ye, Z. Chen, G. Zhang, W. Chen, C. Peng, X. Yang, L. Zheng, Y. Li, X. Ren, H. Cao, *Energy Environ. Sci.* **2022,** *15*, 760-770.

[24] M. Jiang, J. Su, X. Song, P. Zhang, M. Zhu, L. Qin, Z. Tie, J.-L. Zuo, Z. Jin, *Nano Lett.* **2022**, *22*, 2529-2537.

[25] Q. Liu, L. Xie, J. Liang, Y. Ren, Y. Wang, L. Zhang, L. Yue, T. Li, Y. Luo, N. Li, *Small* **2022**, *18*, 2106961.

[26] H. E. Kim, J. Kim, E. C. Ra, H. Zhang, Y. J. Jang, J. S. Lee, *Angew. Chem. Int. Ed.* **2022,** *61*, e202204117.